CHEMISTRY OF MATERIALS

pubs.acs.org/cm

Article

Open Access

This article is licensed under CC-BY-NC-ND 4.0

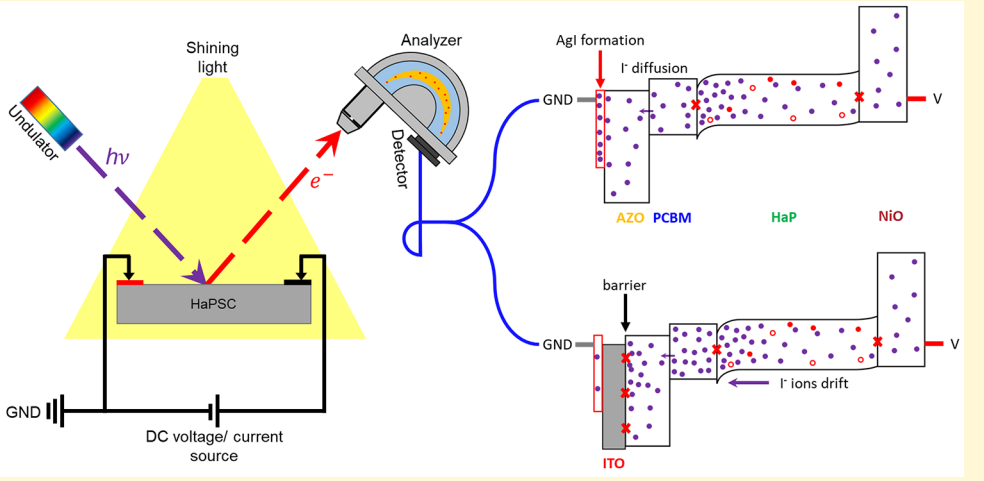
Analysis of Iodide Transport on Methyl Ammonium Lead Iodide Perovskite Solar Cell Structure Through Operando Hard X-ray Photoelectron Spectroscopy

Ibrahima Gueye,* Yasuhiro Shirai,* Takahiro Nagata, Takashi Tsuchiya, Dhruba B. Khadka, Masatoshi Yanagida, Okkyun Seo, Kenjiro Miyano, and Osami Sakata*

Cite This: *Chem. Mater.* 2023, 35, 1948−1960

Read Online

ACCESS | Metrics & More | Article Recommendations | Supporting Information



ABSTRACT: To analyze the dynamic of ion species through a $MAPbI_{3-x}Cl_x$ (HaP) solar cell, an operando hard X-ray photoelectron spectroscopy (HAXPES) study was proposed. Stacked Au/Ag/AZO/PCBM/HaP/NiO/ITO/glass structures, where AZO, PCBM, NiO, and ITO stand for Al-doped zinc oxide, phenyl-C61-butyric acid methyl ester, nickel oxide, and indium tin oxide, respectively, were evaluated. Experimental core level analysis under an applied bias voltage highlighted that a certain threshold voltage (above the open-circuit voltage (V_{OC})) is required to trigger the iodide (I^-) migration from the HaP to the adjacent electron and hole transport layers. Study also demonstrated that the diffusion of I^- in AZO/PCBM over time is unidirectional and follows the gradient descent in concentration. We observed that the irreversibility of the I^- transport leads to the absorption of I^- by the Ag layer to form a silver iodide (AgI) compound. Furthermore, this work also pointed out the efficiency of an ITO layer when deposited between Ag and AZO to serve as the ion diffusion barrier layer. Finally, the results demonstrated that the presence of ITO restrains the AgI formation and contributes to improving cell performances.

1. INTRODUCTION

Recently, hybrid organic−inorganic halide perovskites (HaP) have emerged as one of the most promising materials for low-cost fabrication and high-power conversion efficiency (PCE) in solar cell (SC) technology.[1−4] Besides the tremendous research effort,[5] the dazzling success of HaP is made possible by their intrinsic high light absorption coefficients,[6] long carrier diffusion lengths, extended charge carrier lifetimes,[7] and excellent defect tolerance.[8] HaP structures generally refer to a class of materials with the chemical formula ABX_3, where A is a monovalent cation (methylammonium (MA^+), formamidinium (FA^+), or cesium, etc.), B is a divalent metal cation (Pb^{2+}, Sn^{2+}, etc.), and X is occupied by a halide counterion (Cl^-, Br^-, or I^-).[9] So far, the methylammonium lead iodide ($MAPbI_3$) is the most widely studied member of HaP and is often used as a reference compound.[10] Currently, the highest PCE of a HaP solar cell (HaPSC) has reached 25.7%,[11] exceeding the record efficiency of copper indium gallium selenium (CIGS) and approaching the best record of their silicon counterpart. However, their stability

Received: October 17, 2022
Revised: January 30, 2023
Published: February 22, 2023



ACS Publications

© 2023 The Authors. Published by American Chemical Society

Downloaded from pubs.acs.org/cmatex/article-pdf/35/5/1948/2748132/cm2c03162.pdf by NATL INST FOR MATLS SCIENCE (NIMS) user on 10 November 2026

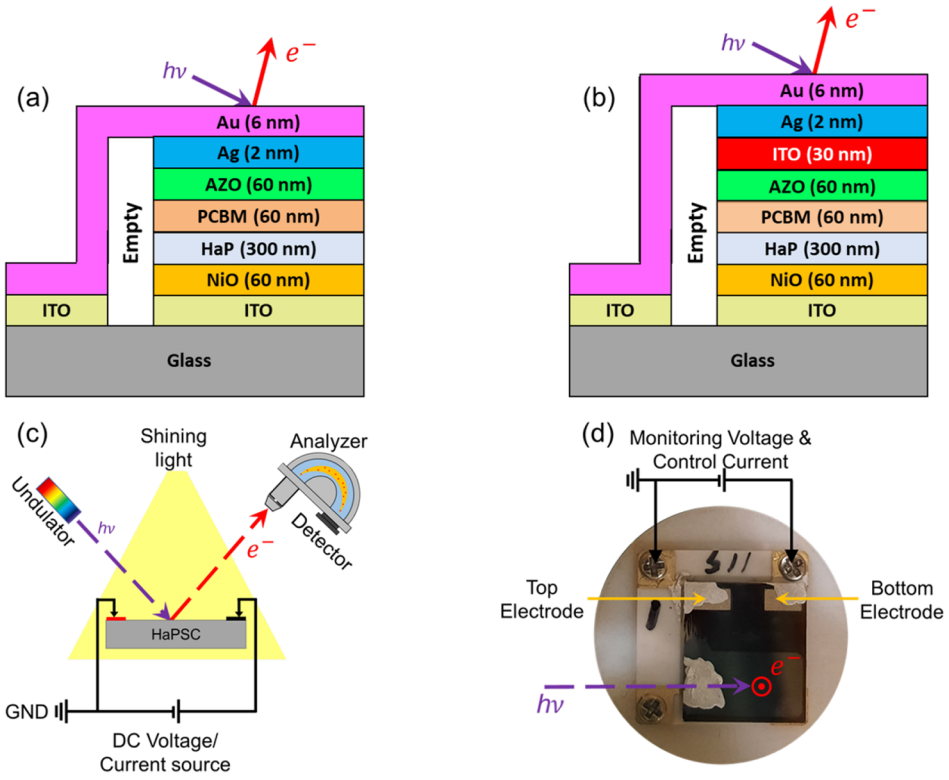


Figure 1. Schematic representation of stacked HaPSC devices used in this work: (a) SP_1 (Au/Ag/AZO/PCBM/HaP/NiO/ITO/glass) and (b) SP_2 (Au/Ag/ITO/AZO/PCBM/HaP/NiO/ITO/glass). (c) Simplified operando HAXPES analysis setup under bias voltage based on synchrotron X-rays. (d) Top view of attached HaPSC sample on a connected HAXPES sample holder for the operando measurement.

issues remain a major bottleneck and restrict HaPSC production for mass commercialization.[12]

Ionic transport inducing an irreversible degradation of HaPSC has been identified as one of the factors that seriously impeded the long-term stability[13] and performances[14−16] of HaPSCs. The easy self-release of ionic compounds during prolonged operation of SCs induces a lot of defects in the HaP layer that serve as nonradiative recombination centers. These remaining defects are also sensitive to moisture and oxygen, which accelerate device decomposition. However, the types of mobile species as well as the dynamic behavior of these latter are still under debate.

In view of the cohesive energy weakness of the flexible crystal lattice of the HaP structure (based on ionic bonds, hydrogen interactions, and van der Waals forces), various types of fragments/defects can be generated as a result of the easy dissociation of the HaP structure.[5] From the most investigated $MAPbI_3$ absorber, the existence of fragments/defects such as interstitials (I_i^-, MA_i^+, and Pb_i^{2+}), vacancies (V_I^+, V_{MA}^-, and V_{Pb}^{2-}), cation substitutions (MA_{Pb}^-), and antisite substitutions (I_{Pb}^{3-}, I_{MA}^{2-}, and Pb_I^{3+}) were predicted.[17,18] Furthermore, on the basis of their activation energy (EA) values, some of them were identified as being accountable for ionic migration. Eames et al. reported three different ionic transports mediated by three different vacancy defects: (i) iodide (I^-) migration along octahedron edges (V_I^+); (ii) MA^+ migration into a neighboring vacant A-site cage (V_{MA}^-); and (iii) Pb^{2+} migration along the <110> diagonal of the cubic unit cell (V_{Pb}^{2-}).[19] The corresponding EA values of the migrating species derived from the first-principles calculation are 0.58, 0.84, and 2.31 eV, respectively. However, in spite of the small EA for both I^- and MA^+, the estimation of their diffusion coefficient at 320 K suggests a negligible transport of MA^+ in comparison to I^-. This dominant I^- transport is due to its much higher overall diffusivity ($\sim 10^{-12}$ cm^2/s) compared to that of MA^+ ($\sim 10^{-16}$ cm^2/s). As for the ion transport mechanism under an applied electric field through the HaP, Huang and co-workers[20] showed that a small electric field of ~ 1.2 V/μm in $MAPbI_3$ can drive the movement of ions, leading to n-type and p-type doping near the anode and cathode, respectively. They also pointed out a massive I^- anion drift during the reversible conversion between the $MAPbI_3$ and PbI_2 phases induced by the bias stress.

From the viewpoint of the actual whole HaPSC devices including adjacent selective contacts, transport layers, and metal electrodes, it still remains unclear that the ion transport itself leading to an insufficient supply of iodine into the HaP film is the exclusive cause of poor performance and instability as evoked by Weber et al.[21] First, we point out that aiming to improve the open-circuit voltage V_{OC} value of an SC requires identification of the straightforward connection between the V_{OC} deficit and the nonradiative recombination losses of the photogenerated charges at interfaces and/or metal contacts in addition to the radiative recombination in the HaP bulk. Ideally, the internal quasi Fermi level splitting (QFLS) in the HaP absorber should be totally equal to the V_{OC} and only limited by radiative recombination in the bulk. However, as the key factor for the efficiency of an SC, the actual V_{OC} always takes into account the overall quality of the cell, which includes imperfections from the interfaces and other stacked layers as well. Therefore, V_{OC} measurement in the actual full HaPSC as a function of the external voltage should provide information regarding the extent to which the situation differs from the ideal case.

Then, recently, several experimental and theoretical studies have brought out the impact of the nonradiative recombination

https://doi.org/10.1021/acs.chemmater.2c03162
Chem. Mater. 2023, 35, 1948−1960

Downloaded from pubs.acs.org/cmatex/article-pdf/35/5/1948/2748132/cm2c03162.pdf by NATL INST FOR MATLS SCIENCE (NIMS) user on 10 November 2026

loss process on solar cell performance.[22−27] Sood et al.[28] and Stolterfoht et al.[29] have highlighted a clear V_{OC} deficit ($V_{OC,def}$) between the internal V_{OC} ($V_{OC,in}$) measured by optical (photoluminescence (PL)) measurements and the external V_{OC} ($V_{OC,ex}$) from electrical (current−voltage ($I-V$)) measurements. In fact, the $V_{OC,in}$ from PL is calculated from the ratio of the total radiative recombination flux of the device to the flux of injected photons and provides a direct measure of the intrinsic quality of an absorber. In this regard, $V_{OC,in}$ reflects the real QFLS from the bulk perovskite, while the $V_{OC,ex}$ from $I-V$ indicates an energetic difference between the hole quasi-Fermi at the hole contact and the electron quasi-Fermi at the electron contact.

Moreover, we finally point out that ion motions across selective/transport layer materials[30] and metallic electrodes[31] under long-term operation, especially for the benchmark $MAPbI_3$ device, could result in chemical reactions as well as the formation of an interfacial ion accumulation layer and the modification of the energy band alignment across interfaces.[36−38] From our earlier work related to the interfacial chemistry of $MAPbI_{3-x}Cl_x$/transport layer materials,[32] we confirmed that chemical degradation mainly exists at the interface between the materials. From this same report, we also point out an accumulation of iodine species in the organic electron (phenyl-C61-butyric acid methyl ester (PCBM)) and hole (poly[bis(4-phenyl)(2,4,6-trimethylphenyl)amine] (PTAA)) selective layers after the self-release from the bulk absorber $MAPbI_{3-x}Cl_x$. Furthermore, the I^- consumption by the metallic electrode affecting the PCE was previously pointed out by Kato et al.[33] and Cheng et al.[34] Following the approach of Boyd et al.,[35] by using an ITO layer as a potential barrier layer between the transport layer material and the metallic electrode, we note an increase of the current density and the PCE (from 11.5% to 12.4%), as seen in the Supporting Information (Figure S1). Therefore, it seems necessary to shine more light on some chemical changes operated in layers and buried interfaces through the use of a suitable analysis tool.

Photoelectron spectroscopy (PES) based on soft X-rays[39,40] possesses all abilities to study the valence band structure as well as the chemical states and relative concentrations of constituent elements of samples. However, in a nondestructive analysis, soft PES often fails to provide bulk and buried interface features due to its large surface sensitivity. Hard X-ray photoelectron spectroscopy (HAXPES)[41−43] offers an immense opportunity to investigate up to several tens of nanometers depth without any damage on the samples. Taking this into account, here we present one methodology to directly track down, over a several nanometer scale, the dynamics of ion species inside $MAPbI_{3-x}Cl_x$ (HaP)-based SC devices under an operating condition. From this operando HAXPES analysis under an applied bias voltage, we will also focus on the impact of the ITO interlayer proposed as the barrier against the harmful ionic migration.

2. EXPERIMENTAL SECTION

2.1. Materials and Preparation. Two stacked solar cells without and with an ITO interlayer labeled as SP_1 (Au/Ag/AZO/PCBM/HaP/NiO/ITO/glass) and SP_2 (Au/Ag/ITO/AZO/PCBM/HaP/NiO/ITO/glass), respectively, as seen in parts a and b of Figure 1, were manufactured during this work. To grow both samples, a nickel oxide (NiO) layer was deposited as a hole transporting layer (HTL) on a precleaned patterned ITO-coated glass substrate by radio frequency (RF) sputtering at room temperature. The target NiO was sputtered under an argon gas pressure of 3.5 Pa with an RF power supply of 50 W. Then, the samples were transferred inside the glovebox for the 300-nm-thick HaP film deposition.

For the HaP preparation, first a PbI_2 precursor solution was spin-coated at 3000 rpm for 90 s. Then a mixed precursor solution of methylammonium iodide (MAI) and methylammonium chloride (MACl) was spun onto the PbI_2 layer at 4000 rpm for 30 s to obtain the HaP ($MAPbI_{3-x}Cl_x$) layer.[44] To crystallize the HaP film, we placed samples on a hot plate with MACl powder covered with a Petri dish at 100 °C.[45] PCBM (60-nm-thick) used as an electron transport layer (ETL) was spin-coated over the HaP films at 700 rpm for an initial 30 s and 5000 rpm for 10 s. The PCBM layer was thereafter annealed at 100 °C for 5 min on the hot plate. Subsequently, a 60-nm-thick AZO buffer layer was further spin-coated at 1000 rpm for 5.5 s coupled with 4000 rpm for 20 s followed by annealing on the hot plate at 100 °C for 10 min.

Prior to the last step of the SP_2 sample fabrication, 30-nm-thick ITO was sputtered at an Ar pressure of 0.15 Pa and a dc power supply of 50 W at room temperature. Finally, the Au/Ag (6 nm/2 nm) bimetallic electrodes were thermally evaporated successively on top of the AZO for SP_1 and ITO for SP_2 to complete the cell structures. We note that the normal solar cell structure uses a thicker layer of bimetal top electrodes; however, for this HAXPES analysis we have intentionally used the thinner Au/Ag bielectrode layer to be able to get chemical information from the buried layers. The active area (electrode size) of the devices is 0.26 mm^2.

After the whole deposition processes were complete, SP_1 and SP_2 samples were kept in an N_2-filled box throughout the transport steps to avoid any oxygen or moisture contamination. To maintain a high purity of the working environment before introducing samples into the HAXPES analysis chamber, an argon-filled glovebag was used to manipulate the samples. After placing both samples on the sample holder, these latter were again stored in a special argon-filled box that was connected to the transfer chamber of the HAXPES machine.

2.2. Device Characterization. HAXPES analyses were carried out at BL15XU beamline at SPring-8 synchrotron facility (Japan).[46] Basically, the synchrotron facility provides a very intense beam of high-energy X-rays, a million times more intense than laboratory-based X-ray systems, and therefore has a much higher depth of penetration. With their short wavelength (comparable to the size of atoms) and high energy, hard X-ray photons can penetrate tens to hundreds of micrometers into most materials.[47−49] Intuitively, they can pass through our relatively thin stacked Au/Ag/ITO/AZO/PCBM/HaP/NiO structures, which are <0.6 μm. A generic description of the operando HAXPES setup is depicted in Figure 1c. In this investigation, all analyses were performed at room temperature and a stable base pressure (~10^{-7} Pa).

Linearly polarized X-rays in the horizontal plane were used to conduct all of our measurements. Considering that the angle between the incoming X-ray beam and the photoelectron analyzer is 90°, for almost all measurements the X-ray beam was incident on the samples with a grazing angle of 5°; thus, the photoelectrons were collected along directions close to the normal to the surface at 85°. This experimental geometry with a takeoff angle (TOA = angle between the surface sample and the HAXPES analyzer) of 85° was chosen to favor the bulk sensitivity as much as possible. In this configuration, a projected X-ray beam with an expanded footprint size of approximately 400 × 30 μm^2 at the sample surface was used. The excitation photon energy during all measurements was set to 5.95 keV, and photoelectrons were detected and analyzed with a hemispherical electron analyzer (VG-Scienta R4000) in the angle integrated transmission mode with an acceptance angle of ±7°. The total energy resolution (photon and spectrometer bandwidths) was estimated to be 0.24 eV as determined by fitting the Au Fermi edge. The binding energy (BE) was calibrated by using the Fermi edge of an evaporated Au film.

On the basis of the theoretical inelastic mean free paths (IMFPs) calculated by the QUASES-IMFP-TPP2M software,[50] the sampling depth (d) or escape depths of photoelectrons ($d \approx 3 \times$ IMFP $\times$ sin(TOA)) were roughly estimated at ~30 nm for the photon energy of 5.95 keV used in this work. We draw attention to the fact that, with the

Downloaded from pubs.acs.org/cmatex/article-pdf/35/5/1948/2748132/cm2c03162.pdf by NATL INST FOR MATLS SCIENCE (NIMS) user on 10 November 2026

https://doi.org/10.1021/acs.chemmater.2c03162
Chem. Mater. 2023, 35, 1948−1960

high density of the Au top electrode (~19.3 g/cm^3), the actual information depths may be slightly lower than 30 nm.

For the treatment of HAXPES data, CasaXPS (CASA Software, Ltd.[51]) was mainly used. To be more specific, core levels were fitted using a pseudo-Voigt peak shape (Gaussian/Lorentzian) with a Shirley algorithm to model the background subtraction as primarily needed. The Lorentzian contributions for the investigated core levels were small and were kept fixed at the same width for the fitting of one core level.

An ADCMT 6241A DC Voltage−Current Source/Monitor system interfaced with an external computer controller located outside the experimental hutch was used to apply different bias voltages on samples during measurements, as illustrated in Figure 1d. A dc bias signal was applied to the ITO bottom electrode, whereas the Au top electrode was grounded to eliminate any surface charge contribution. Note that all analyses were conducted under an identical room light (~300 lx) condition corresponding to 0.1 mW/cm^2 of irradiance. Finally, we underline that HAXPES data recorded for each set of voltage always started after we reached a steady state of the current density (~15−20 min), as depicted in Figure S2a. Throughout this work, each complete HAXPES data recording duration after reaching a stable current density was ~90 min, unless stated otherwise. This length of time (~2 h for each set of voltage: transient state + wide, Au 4f, Ag 3d, Zn 2p, Al 1s, O 1s, C 1s, N 1s, Pb 4f, I 3d, and valence band) is considered as enough duration to observe any significant chemical reaction or intensity variation (diffusion process).

3. RESULTS AND DISCUSSION

To establish the reliability of our reported electric setup from Figure 1d, it was required to ensure that samples in the analysis chamber were appropriately connected to the voltage supply located outside the hutch. Current density−voltage (J−V) measurements before any X-ray exposure (X-ray shutter close) were performed as reported in Figure 2a. SP_1 and SP_2 samples were recorded by scanning in forward (line) and reverse (dashed line) directions. From the J−V results, a hysteresis feature is uncovered in both samples (but is more significant in the SP_2 sample). Furthermore, we highlight the effectiveness of the ITO interlayer with the notable enhancement of the current density when comparing the SP_1 and SP_2 responses.

V_{OC} responses from the SP_1 and SP_2 samples over time are reported in Figure 2b. The outcomes display the direct impact of the synchrotron X-ray beam exposure on the V_{OC} response when several on/off switching cycles of the X-ray beam (open and close operation mode) were performed. The beam shutter open (or close) on demand are used to selectively transmit (or block) the X-ray beam at the sample surfaces. Letters O and C are used to refer to the open and close modes of the shutter, respectively. Prior to the first beam exposure (below 0.01 h), the intrinsic positive effect of the ITO interlayer on the V_{OC} is proved by comparing SP_1 (~0.75 V) and SP_2 (~0.80 V) data. Under O mode, an important drop of V_{OC} magnitude occurs and is then followed by a relaxation phase. When switching to the C mode, the V_{OC} pursues its recovering process until reaching the initial V_{OC} baseline value. This procedure was repeated several times to confirm the X-ray impact, as shown from Figure 2b. Furthermore, to provide a satisfactory explanation of J−V and V_{OC} results, we studied the chemical changes that occurred on the samples (survey, Figure S3) following the deposition of the ITO interlayer (Figure S4). Thorough core level analyses were conducted to distinguish the effects of different bias voltage levels on each layer.

Chemical information on the Ag layer from the SP_1 and SP_2 samples is reported in parts a and b of Figure 3, respectively. A similar Ag 3d$_{5/2}$ BE position at the 368.0 eV[52,53] state is detected on both samples. This Ag 3d$_{5/2}$ position is located at a lower BE relative to the Ag^0 metal, expected at 368.3 eV.[54,55] We ascribe this lower BE shift to the formation of the

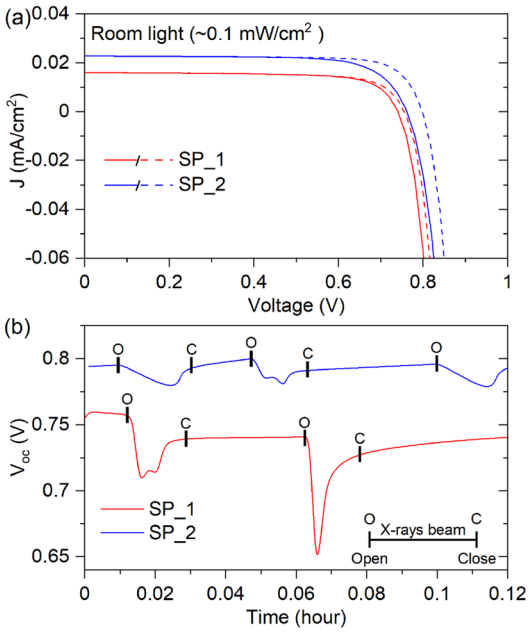


Figure 2. Electric characteristics of SP_1 (red) and SP_2 (blue) samples under room illumination: (a) current density−voltage (J−V) and (b) synchrotron X-ray source impact on the open-circuit voltage (V_{OC}) values, where O and C refer to the open and close operation modes of the shutter, respectively. The shutter open (or close) on demand is used to selectively transmit (or block) the X-ray beam at the surface of the samples.

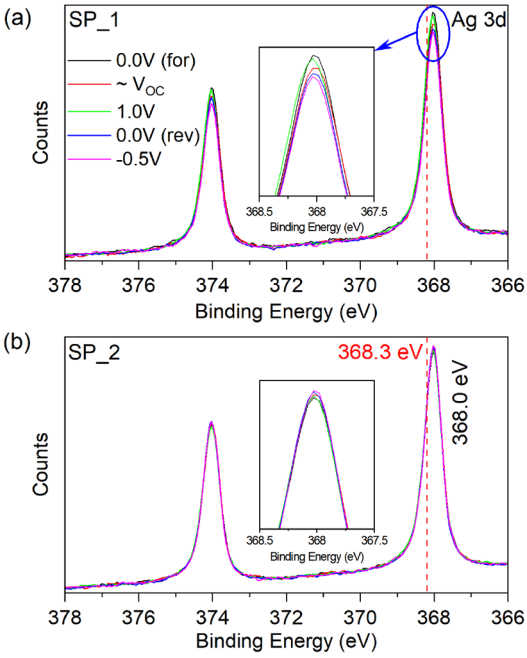


Figure 3. Ag 3d HAXPES core level spectra as a function of the bias voltage applied on the HaPSCs at a takeoff angle of 85°: (a) SP_1 and (b) SP_2 samples. Binding energies at 368.3 and 368.0 eV are related to Ag^0 metal and AgI, respectively. From the insets, we compare the evolution of the maximum intensity of Ag 3d$_{5/2}$ as a function of the applied bias voltage.

Downloaded from pubs.acs.org/cmatex/article-pdf/35/5/1948/2748132/cm2c03162.pdf by NATL INST FOR MATLS SCIENCE (NIMS) user on 10 November 2026

https://doi.org/10.1021/acs.chemmater.2c03162
Chem. Mater. 2023, 35, 1948−1960

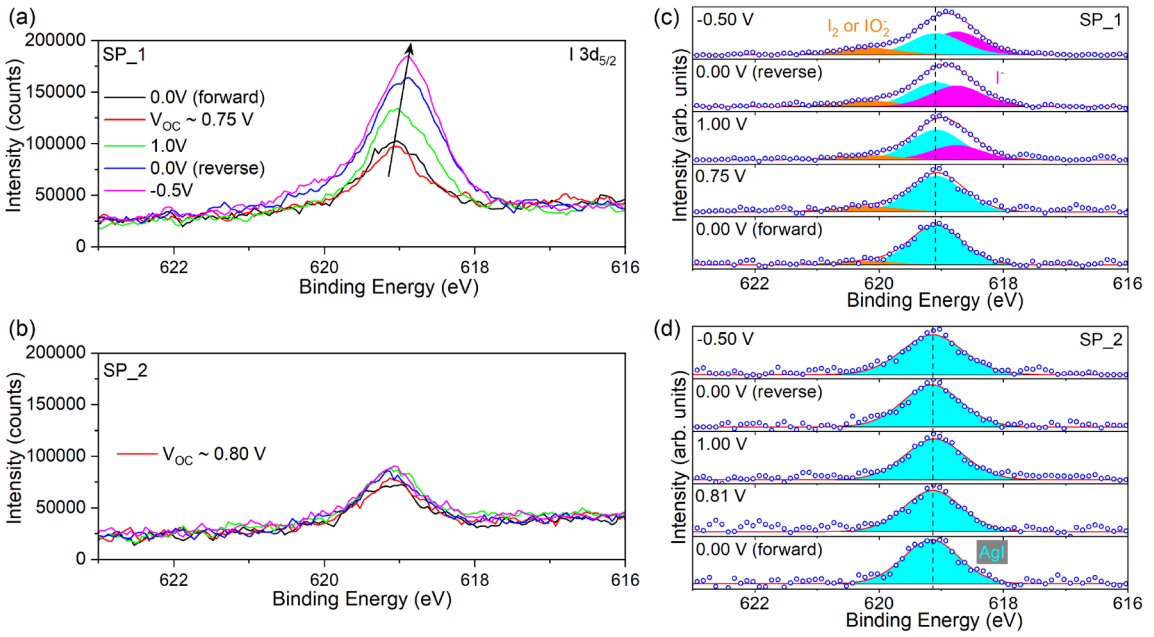


Figure 4. I $3d_{5/2}$ core level recorded at different bias voltages: (a) SP_1 and (b) SP_2. Similar intensity scale and binding energy range are used to compare the intensity changes and energy shifts between the SP_1 and SP_2 samples. Reported data fitting from the I $3d_{5/2}$ core level: (c) SP_1 and (d) SP_2. Vertical dashed lines have been placed to illustrate the clear shift of the envelope of the magenta and orange components.

mixture of Ag with another element such as I^-, as already suggested by Kato et al.[33,56] The AgI signal is of interest as it shows anomalous negative chemical shifts compared to the metal. On the basis of the analysis of diverse initial- and final-state phenomena in the photoelectron spectroscopy, many possible mechanisms can lead to the atypical decrease of the binding energy with the increase of the oxidation state of silver. Gaarenstroom and Winograd attribute this significant negative shift to the initial-state factors of ionic charge and lattice potential,[57] while Bagus et al. associate it to the Madelung potential (which is always negative at a cation site due to surrounding anions).[58] It appears to be the dominant factor in the case of Ag oxides, where positive shift due to electron loss is small and overcome by the significant negative shift due to the Madelung potential. Finally, we underline that this atypical negative binding energy shift also has been highlighted from copper with the Cu $2p_{3/2}$ binding energies of Cu metal and Cu_2O at 932.7 and 932.5 eV, respectively.[59−61] Regarding our study, we assume that the AgI halide results from the reaction between the Ag^+ from the electrode and the I^- escaping from the HaP absorber. Furthermore, another important observation from Figure 3a and b is that the SP_2 maximum intensity remains unaffected, whereas a certain variation of the maximum intensity is detected on the SP_1 sample as a function of the bias voltage. On the basis of this evidence, we suspect an I^- diffusion into the Ag layer[62] (and/or the existence of Ag^+ ion transport toward the HaP side) taking place only without an ITO barrier layer (SP_1 sample). Finally, we note that the similar analyses performed on the grounded gold layer do not show any significant difference between the SP_1 and SP_2 samples (Figure S5), and the corresponding BE of Au $4f_{7/2}$ at 84.0 eV is consistent with the metallic state of the gold (Au^0[54,63]).

Figure 4 reports I $3d_{5/2}$ (~619 eV) core levels depending on the applied bias voltage on samples. With the I $3d_{5/2}$ peaks in Figure 4a, we provide proof that an iodide transport process happens in the SP_1 cell, and this move is also voltage-dependent. Most importantly, the results clearly demonstrate that a certain voltage threshold is required to trigger the iodide migration. In fact, with 0.0 V (forward) and 0.75 V ($\sim V_{OC}$), no significant variation of I $3d_{5/2}$ intensity correlated to an iodide transportation is detected. In this work, we associate a diffusion or migration of iodide species from the HaP toward the Au/Ag bielectrodes with a perceptible increase of I $3d_{5/2}$ intensity. However, we do not identify the slight fluctuation of I $3d_{5/2}$ intensity under 0 V (forward) relative to the $V_{OC} \approx 0.75$ V as a transverse iodine transport from the HaP under voltage. This trivial intensity decrease in the case of V_{OC} is not related to any back-migration of iodide but rather to a minor reorganization or lateral redistribution of iodide species located at the Ag/AZO layers. Furthermore, by applying 1 V (higher that the SP_1 V_{OC}), we witness a drastic increase of the I $3d_{5/2}$ contribution.

To explain our results, first it is important to recall that the same room light exposure (0.1 mW/cm^2) was used during all of this work. Then, the X-ray radiation does not induce or contribute to any iodide transport as demonstrated from the investigation of the X-rays impact reported in Figure S6a and b. Therefore, at 0 V, we can primarily deduct that charge carriers generated inside the HaP layer by only the illumination are not enough to remove the intrinsic energy barrier established at the HaP/PCBM interface. Additionally, we infer that under 0.75 V we only ended up with a decrease of the interfacial energy barrier but not an iodide transport outside the HaP film. As expected at 1 V, the presence of a high electric field across the HaP layer drives the generation of a substantial amount of charge carriers, leading to an interfacial energy barrier cancellation. With this latter configuration, halide species (iodide) can easily cross the HaP/PCBM interface and spread out toward the lower iodide gradient (Au/Ag side).

For 0.0 V (reverse) and −0.50 V, we continuously detect an increase of I $3d_{5/2}$ intensity. From Figure 4a, we report that the relative concentrations from the I 3d core level at 1, 0 (reverse), and −0.5 V are 1.95, 2.4, and 2.7 times higher than that of 0 V

https://doi.org/10.1021/acs.chemmater.2c03162
Chem. Mater. 2023, 35, 1948−1960

Downloaded from pubs.acs.org/cmatex/article-pdf/35/5/1948/2748132/cm2c03162.pdf by NATL INST FOR MATLS SCIENCE (NIMS) user on 10 November 2026

(forward), respectively, which is consistent with a constant transport process. Basically, it was expected to have (i) a reestablishment of the initial energy barrier at 0.0 V (reverse) and (ii) a raise of the energy barrier about $q(-0.5\ V)$ eV at −0.5 V. Thus, no iodide species will be injected into the PCBM, and 0.0 V reverse or −0.50 V bias voltage cannot explain the large I $3d_{5/2}$ intensity. To interpret these observations, we considered the PCBM layer as an iodide tank. This assumption is strongly related to our previous investigation of $MAPbI_{3-x}Cl_x$/transport layer material interfaces where a large amount of iodide species was observed near and inside the PCBM layer after the deposition of this last one.[32] Therefore, by applying 1.0 V, a large amount of iodide species can be stored inside the PCBM film. Then, during the 0.0 V (reverse) and −0.50 V analyses, we witness a continuous diffusion of iodide species toward the Ag side driven by a gradient descent in concentration. We also underline that the −0.50 V process is only time-dependent but not bias-voltage-dependent. To dispel all doubt on whether or not there could be a process of iodide diffusion under −0.50 V, we performed a specific additional short time bias voltage measurement to only follow the I 3d core level evolution, as described in Figure S6c and d. As widely demonstrated in the Supporting Information, −0.50 V does not trigger an iodide transfer from the HAP to the PCBM over the HaP/PCBM energy barrier. The iodide increase is strictly associated with the diffusion due to the descent gradient concentration between the PCBM and the AZO and Ag.

Furthermore, an interesting detail is observed from Figure 4b associated with the ITO barrier layer impact on the out-diffusion iodide elements. No notable increase of the I $3d_{5/2}$ component is observed regardless of the bias voltage applied on the SP_2 sample. The experimental results confirm the effectiveness of ITO to prevent the harmful iodide leakage from the AZO toward the metal electrode. In addition, we report a lower amount of residual iodide species (I $3d_{5/2}$ signal at 0.0 V (forward)) from the SP_2 sample profiling depth conversely to the SP_1 sample at 0.0 V (forward). To describe the mechanism behind the suppression of iodide diffusion with the presence of ITO, we can consider the existence of physical and/or chemical interactions that block the migration toward Ag. First, because the ITO film is amorphous (complete lack of long-range order and grain boundaries), iodide species will not be able to physically progress and cross the ITO layer through the grain boundary channel.[64,65] Besides the influence of the ITO morphology, we also speculate that physical blocking of iodide can be attributed to the establishment of a continuous In−O−In (In−O−Sn) network structure, which can form a physical barrier again the iodide migration. In fact, the In−O bond length of 2.17 Å[66] is smaller than the diameters of iodide species such as the I^- ion (4.12 Å[67,68]), which makes the In−O bond suitable to physically block the iodide progression. Furthermore, regarding the chemical blocking aspect, we suspect the formation of strong In−I or Sn−I and O−I bonds at the AZO/ITO interface, which leads to chemically preventing the iodide diffusion toward the Ag.[69]

Now, to describe the contribution of each chemical state of the I $3d_{5/2}$ peaks from the SP_1 and SP_2 samples, the following aspects were considered during all fitting processes. As shown in parts c and d of Figure 4, the single cyan component at 0 V (forward) was used as the reference. Its binding energy position, shape, and full width at half-maximum (fwhm) were held fixed during the I $3d_{5/2}$ peak fittings of the other four bias voltages. The SP_2 sample spectra consist of only one main peak located at 619.1 eV, as clearly identified from Figure 4d. We ascribed this chemical state to the presence of the AgI interlayer.[70−72] Basically, it is unexpected to observe the existence of the AgI compound from the SP_2 sample because of the presence of an ITO barrier layer. In other words, halide species should not be able to directly reach the Ag layer and create an AgI structure as in the case of the SP_1 sample without an ITO barrier. To describe the presence of AgI on the SP_2 sample, first we believe that the residual Ag−I reaction takes place during the manufacturing process. Indeed, as we observed in our previous report, after the PCBM deposition on the HaP, a certain amount of iodide crossed the interface and moved into the PCBM. It is expected that part of the iodide species located in the PCBM layer will undergo a migration process toward the AZO surface after the deposition of this last one. Thus, during the progressive sputtering of ITO on the HaP/PCBM/AZO, we suspect successive short length vaporization and redeposit at the top of the ITO layer. Therefore, after the Ag deposition on the ITO surface, we end up with residual AgI. Furthermore, we cannot exclude a transfer (vaporization) of iodide elements from the edges of the HaP, as suggested by Boyd et al.[35]

Regarding the analysis of the SP_1 sample in Figure 4c, new components (magenta and orange) were added to achieve a best peak fitting of the experimental results. In SP_1, we assume that the magenta peak at 618.8 eV is associated with the presence of the free iodide element (I^-[73−76]), while the orange signal at 620.2 eV is linked to the I_2[77] or IO_2^-.[78] According to our probing depth length (<30 nm), we estimate that the residual I_2/IO_2^- elements are mainly located at the buried AZO layer. We underline that the IO_2^- formation can be straightforwardly related to the reaction between an I^- from HaP and oxygen species originated from AZO or PCBM ($C_{72}H_{14}O_2$). As for the I_2 generation, we recall that any I_2 signal was observed during our previous investigation of HaP/PCBM interfaces.[32] Therefore, we assume that the I_2 formation can result in an electrochemical oxidation of the I^- ions ($2I^- \rightarrow I_2 + 2e^-$) by the Ag electrode or a partial decomposition of AgI ($2AgI \rightarrow 2Ag + I_2$).[79] Moreover, with the discharge of iodine elements from the HaP to the PCBM at 1 V, iodide species progressively diffuse into the PCBM and then flow until the AZO/Ag interface. This process explains the appearance of free I^- ions (magenta peak). In the cases of 0 V (reverse) and −0.5 V, the growth of I^- signals are only attributed to the migration leading by a gradient of concentration. Finally, we point out that, due to the total absence of Pb 4f and N 1s signals during our operando HAXPES record, we fully exclude a diffusion of PbI_2 and MA^+ fragments from the HaP to the Ag layer.

In this study, the so-called self-healing or retro-diffusion mechanism of iodide toward the HaP layers was also investigated. This hypothetical reverse transport of ion elements by resting the solar cell in the dark is often described as the main cause of a complete recovery of cell performances after the degradation of properties. To get more clarification, the SP_1 sample was remeasured at 0 V after resting it during 72 h at room temperature in the HAXPES analysis chamber. During this storing period, no bias voltage was applied on the SP_1 sample. The impact of the room light (~0.001 sun light intensity) on SP_1 was assumed to be insignificant. This assumption becomes relevant when comparing the low-level current density generated under normal room light (Figure 2a) to the high current density recorded under AM1.5G (100 mW/cm^2 in Figure S1) conditions.

Downloaded from pubs.acs.org/cmatex/article-pdf/35/5/1948/2748132/cm2c03162.pdf by NATL INST FOR MATLS SCIENCE (NIMS) user on 10 November 2026

https://doi.org/10.1021/acs.chemmater.2c03162
Chem. Mater. 2023, 35, 1948−1960

As reported in Figure S7, we observe the increase of I $3d_{5/2}$ intensity subsequently to the resting time. Figure 5 shows the

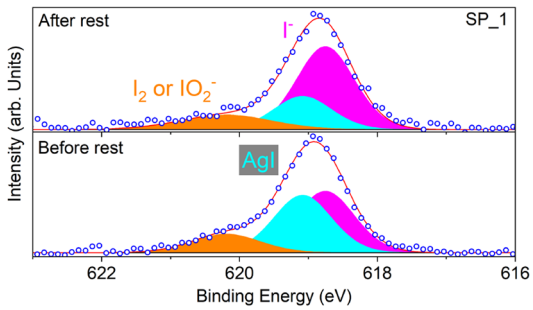


Figure 5. Investigation of the resting phase on the iodide migration of the SP_1 solar cell. Comparison peak fitting of I $3d_{5/2}$ core level from SP_1 before and after resting. Note that the resting step during 72 h takes place after the −0.5 V HAXPES analysis.

comparison of I $3d_{5/2}$ peak fitting spectra obtained prior (last measure at −0.5 V before 72 h of storage) and post (measurement at 0 V after 72 h of storage) storage period at 0 V. Data analyses indicate an increase of the I^- signal after 72 h. We underline that this fact is not consistent with a self-healing process associated with an iodide transport back to the HaP layer. This observation is coherent with a progressive move of I^- toward the Ag/AZO interface. In addition, we remark that the absorption of iodide by the Ag layer to form the AgI (cyan) component seems to reach a certain limit. Thus, by varying the thickness of the Ag electrode from 2 to 10 nm, we do not observe anymore the presence of the I^- compound when the I 3d intensity increases with the bias voltage, as seen in Figure S8. These results demonstrate that the rate of AgI formation or reaction strongly depends on the thickness of the Ag metal electrode. Thus, when a certain threshold of absorption is reached with 2-nm-thick Ag, the excess of I^- coming from the PCBM and AZO does not react anymore with Ag to generate the AgI structure. Therefore, the remaining ionic I^- will be accumulated at the Ag/AZO interface.

On the basis of earlier results, the iodide ions distribution through the whole solar cell device before and after the rest time will depend on the thickness of the Ag if no ITO barrier layer is used. With a thin Ag layer (2 nm), we have a progressive diffusion from the higher concentration of iodide (PCBM side) to the lower iodide concentration (Ag). Due to the generation of the AgI compound, the iodide will be steadily absorbed until the Ag layer reaches its maximum limit of consumption. When the Ag is saturated, the iodide will start to be accumulated at the Ag/AZO interface as well as in the AZO. This situation will likely reduce the gradient between AZO and PCBM, which also reduces the rate of diffusion of iodide. Indeed, the speed of diffusion depends on the gradient in iodide concentration all along the stacked Ag/AZO/PCBM. We expect that for a long rest time the system will reach an identical iodide concentration between the AZO and the PCBM. Then with the use of thick Ag, only the AgI amount will increase until it reaches a corresponding limit of consumption, and then we observe again an accumulation process at the Ag/AZO interface as well as in the AZO. Furthermore, with the presence of an ITO barrier, we infer that all iodide will be stored between the AZO and PCBM layers. We also expect that the diffusion of iodide from the HaP at high voltage (over the threshold voltage) will continue until the iodide concentration between the AZO/PCBM and HaP as well as NiO layers reaches an equilibrium (same concentration). Finally, the fact that we observe a gradient of diffusion over time suggests that, by intentionally doping the AZO/PCBM and eventually the NiO with iodide during the deposition process, we may reduce or cancel the detrimental transfer (loss) of iodide from the HaP to the transport layers under high bias voltage.

In regard to the accumulation of I^- ions around the Ag/AZO interface, the chemical state of AZO from SP_1 was studied as a function of the applied voltage (Figure S9). Besides the expected AZO band bending effect under bias stress, the Zn $2p_{3/2}$ core level has kept similar features as seen in Figure 6. Moreover, one can consider that the porous aspect of the AZO layer[80] likely favors easy absorption, accumulation, and even transport of I^- species.

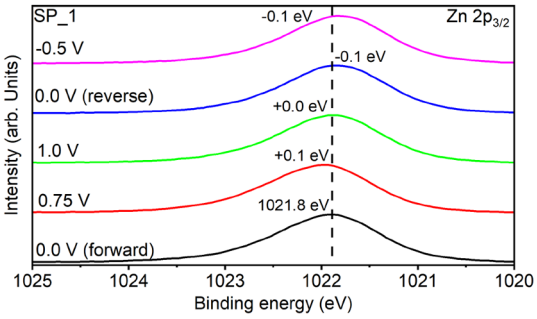


Figure 6. Analysis of the chemical change that occurred in the AZO layer in the SP_1 solar cell sample: Zn $2p_{3/2}$ core level recorded at different bias voltages during the operando HAXPES analysis.

To propose models that illustrate the iodide transport in whole cells, additional valence band information from ITO-, NiO-, HaP-, PCBM-, and AZO-bare was recorded, as seen in parts a−e of Figure 7, respectively. We note that for these measurements each bulk layer deposited on an ITO substrate was separately measured. The experimental valence band maximum (VBM) obtained by using a linear extrapolation[81] and the theoretical bandgaps are also included in Figure 7. Schematic band diagrams of each layer before contact are summarized in Figure S10. We underline that experimental valence band structures from the actual SP_1 and SP_2 samples dominated by the grounded Au metal signal do not provide any significant indication as seen in Figure S11 and cannot really help to build our following model.

Figure 8 reports a graphic illustration of the band structure of stacked AZO/PCBM/HaP/NiO after the initial contact of layers. At that equilibrium, state drift and diffusion of mobile species are equal but opposite at all points in the HaP structure. Typically, a short time prior the stacked PCBM/HaP/NiO contact is established, and a built-in electric field resulting from the difference of Fermi levels takes place. This built-in potential drops linearly between the NiO and PCBM equilibrate the Fermi level across the HaPSC, as depicted in Figure S12. The mechanism will trigger a migration of iodide species toward the PCBM while immobile vacancies or defects remain fixed (not shown in the schemes). This iodide transport process leads to the creation of a halide-accumulation region close to the PCBM and enhances the band bending of the HaP near the PCBM/HaP interface. The ionic electric field generated by the accumulation of iodide ions will screen the internal built-in electric field at the PCBM/HaP edge. Thus, at the equilibrium

Downloaded from pubs.acs.org/cmatex/article-pdf/35/5/1948/2748132/cm2c03162.pdf by NATL INST FOR MATLS SCIENCE (NIMS) user on 10 November 2026

https://doi.org/10.1021/acs.chemmater.2c03162
Chem. Mater. 2023, 35, 1948−1960

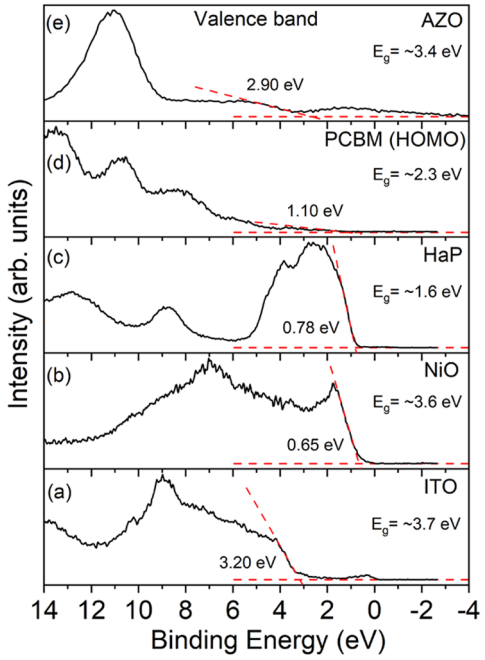


Figure 7. Valence band spectra measured from the (a) ITO-bare, (b) NiO-bare (NiO/ITO), (c) HaP-bare (HaP/ITO), (d) PCBM-bare (PCBM/ITO), and (e) AZO-bare (AZO/ITO). For each sample a linear extrapolation method is used to obtain the valence band maximum value as depicted by the red dotted lines. All energy band gaps are acquired from the literature.

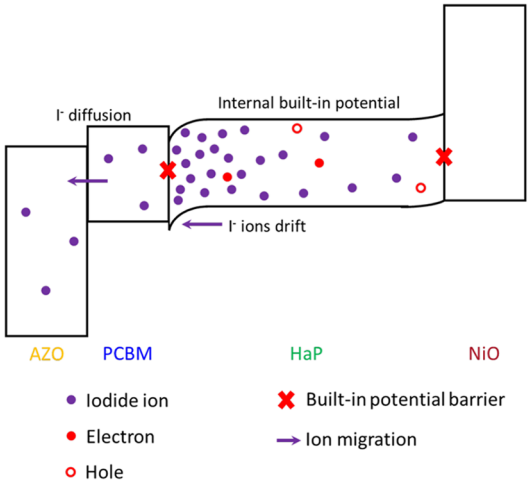


Figure 8. Schematic illustration of AZO/PCBM/HaP/NiO energy band diagram at equilibrium after contact and before the operando HAXPES analysis under an applied bias voltage. The mobile iodide ions are symbolized by violet-filled circles, and the violet arrow indicates the direction of iodide transport. Red empty circles and red filled circles represent the holes and electrons, respectively. Charge carriers (holes and electrons) are generated by both the light and the voltage. The red cross symbol corresponds to the presence of a barrier against the diffusion of iodide.

state, a net built-in electric field will take place in both edges of the HaP to prevent mobile ions from crossing interfaces, as indicated by the red cross symbol in Figure 8. We note that the red empty circles and red filled circles are associated with the residual holes and electrons generated under illumination, respectively.

Figure 8 also brings further clarification about the presence of the residual AgI component previously observed at 0 V (forward) in Figure 4. Indeed, during the iodide accumulation step, a small amount of iodide species escapes from the PCBM/HaP interface and diffuses until the AZO surface. In the case of the SP_1 sample, the silver directly sucks the iodide elements from the AZO to form AgI, while the appearance of residual AgI in the case of the SP_2 sample is attributed to the volatility of iodide during the sputtering process of ITO before the Ag deposition.

Figure 9 schematically summarizes the proposed iodide transport process and band structure evolution of the SP_1 and SP_2 samples during the HAXPES analysis under different bias voltages inferred from the experimental data presented earlier. From the SP_1 model at 0 V (forward) in Figure 9a, the following observations can be highlighted: (1) the presence of a tiny amount of charge carriers generated in the HaP film by the light exposure; (2) the accumulation of iodide species and enhanced band bending near the PCBM/HaP interface, which is implicitly balanced by an important part of iodine vacancies at the HaP/NiO interface (not drawn here); (3) the existence of potential barriers (red cross) at the HaP edges; and (4) the formation of the AgI compound. By applying 0.75 V (Figure 9b), an increase of charge carriers and the modification of the band bending structures between the NiO and the PCBM will take place. This situation drives a partial move of mobile iodide species in the reverse direction (toward the NiO side) and slightly reduces the bending of the HaP band. However, a net energy barrier at the PCBM/HaP interface is still present at 0.75 V, and no iodide species will cross the PCBM/HaP junction.

Under +1 V, the injection of sufficient charge carriers associated with a modification of the band structure of HaP leads to the cancellation of the interfacial energy barrier. The vanishing of the barrier will trigger the migration of iodide species into the PCBM layer, as depicted in Figure 9c. Then, with the existence of the gradient descent of iodide concentration outside the HaP, iodide elements will continue to be distributed toward the AZO/Ag interface. As demonstrated earlier the consumption of iodide by the Ag will solely depend on the Ag thickness; the thicker the Ag layer, the more important is the iodide reaction with Ag to form AgI. Furthermore, without energy barriers at the HaP edges, we do not exclude a diffusion of iodide into the NiO layer. As already suggested by Khadka et al.[82] and Thampy et al.,[83] the chemical reaction between the iodide and Ni^{3+}/Ni^{2+} may likely induce the formation of NiI_2.

At 0 V (reverse) and −0.5 V conditions, we witness the reestablishment of the energy barrier as well as the enhanced band bending of HaP and a reduction of the generated charge carriers. Obviously, the negative voltage is expected to raise barrier potentials and accentuate more band bending effect. Finally, we observe both a reaccumulation of iodide elements at the PCBM/HaP interface and a progressive iodide diffusion processes toward the Ag/AZO junctions.

Furthermore, parts f−j of Figure 9 depict the impact of the ITO (in gray) inserted in the SP_2 sample. We underline that the ITO prevents only the AgI formation but not the iodide migration from the HaP to the AZO layer as well as its accumulation at the ITO/AZO interface. With the ITO, we can also consider that the iodide migration from HaP to AZO will stop when all parts of the stacked AZO/PCBM/HaP reach the same iodide concentration.

Downloaded from pubs.acs.org/cmatex/article-pdf/35/5/1948/2748132/cm2c03162.pdf by NATL INST FOR MATLS SCIENCE (NIMS) user on 10 November 2026

https://doi.org/10.1021/acs.chemmater.2c03162
Chem. Mater. 2023, 35, 1948−1960

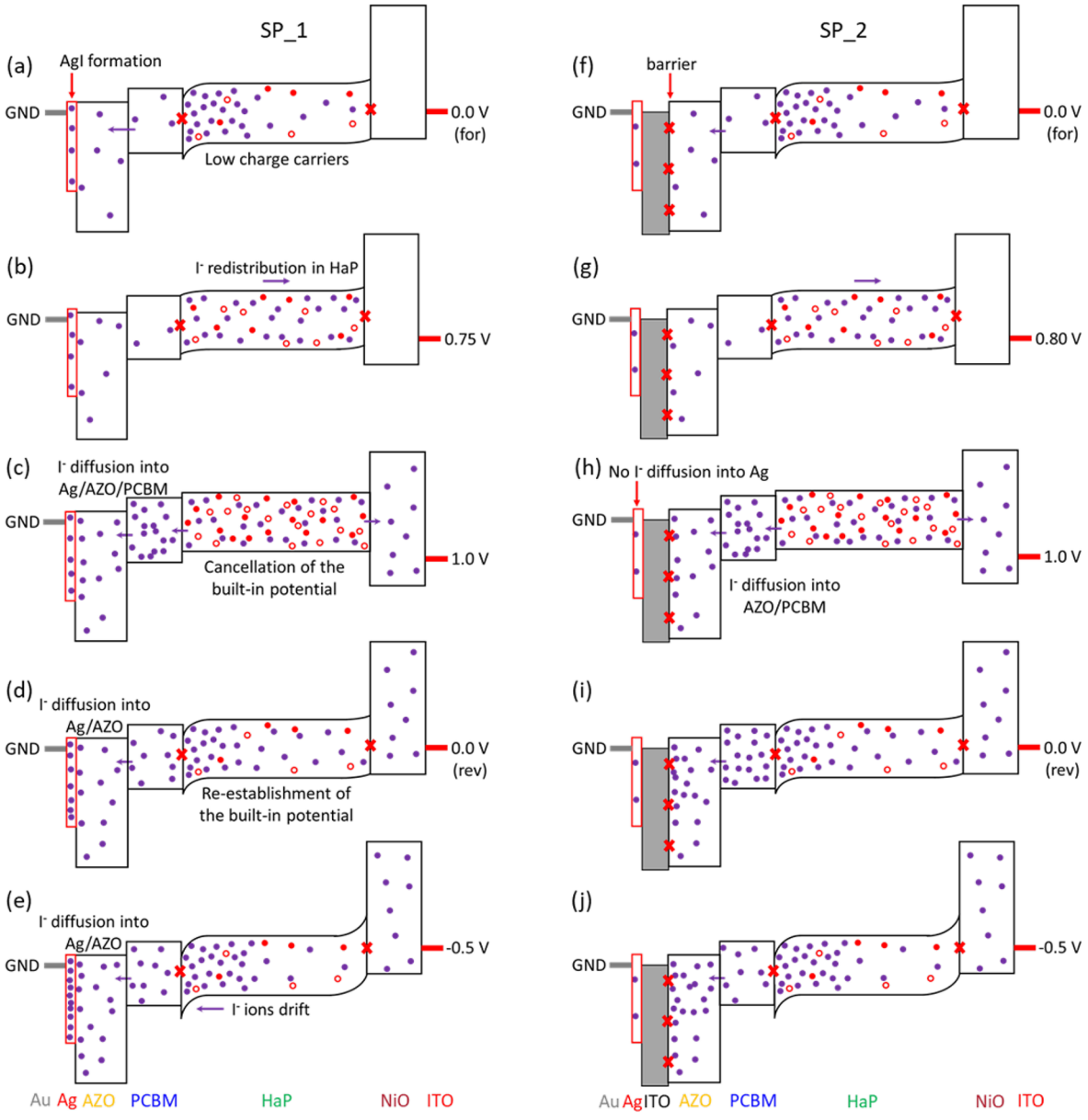


Figure 9. Schematic representative energy band diagram model of samples under applied voltage and room light: (a−e) SP_1 without ITO and (f−j) SP_2 with ITO. The mobile iodide ions are symbolized by violet-filled circles, and the violet arrow indicates the direction of iodide ions migration. A AgI interlayer is present in both SP_1 and SP_2. Au metal was grounded, and the bias voltage was applied on the bottom ITO electrode. Red empty circles and red filled circles represent the holes and electrons, respectively. Charge carriers (holes and electrons) are generated by both the light and the voltage. The red cross symbol corresponds to the presence of a barrier against the diffusion of iodides.

On the basis of these chemical investigations, we can clearly explain some electric features observed earlier in Figure 2. First, an important iodide accumulation inside the AZO due to the ITO barrier layer will attenuate the liberation from the HaP as well as the diffusion toward the gradient descent in concentration of iodide elements. This explanation supports the improvement of the PCE and current density observed with the presence of ITO in the case of SP_2. Furthermore, we associated the enhanced $J-V$ hysteresis feature in the case of the SP_2 sample, as reported in Figure 2a, to iodide ions from and confined at the ITO/AZO interface. In fact, we point out that the anomalous $J-V$ hysteresis behavior is mainly attributed to the existence of capacitive current, charge trapping, and/or interfacial band bending.[84,85] The capacitive effect in SP_2 can be related to a polarization of the ITO/AZO interface due to the ionic accumulation, conversely to the SP_1 where iodide species are progressively sucked directly by the Ag layer until saturation of this last one. Thus, a dielectric relaxation linked to a slow redistribution process of mobile iodide ions under an external electric field can contribute to the $J-V$ hysteresis. Furthermore, the accumulation of mobile ions at ITO/AZO interface can also screen the built-in electric field and alter the band bending structure at the interface. Thus, under an electric field, the slow process of these mobile interface charges will modify the net built-in electric field, which results in $J-V$ hysteresis. We also consider that the dynamic trapping and detrapping processes at

https://doi.org/10.1021/acs.chemmater.2c03162
Chem. Mater. 2023, 35, 1948−1960

Downloaded from pubs.acs.org/cmatex/article-pdf/35/5/1948/2748132/cm2c03162.pdf by NATL INST FOR MATLS SCIENCE (NIMS) user on 10 November 2026

the interface will also contribute to the hysteresis feature. We underline that the discrepancy of the performance between two voltage-sweeping directions when performing a $J-V$ measurement presents a big challenge for determining the actual power conversion efficiency of cells.

Finally, we ascribe the substantial V_{OC} drops reported for SP_1 to the existence of significant interfacial defects/traps and undesirable AgI complex at the Ag/AZO heterojunction, as reported in Figure 2b. Under X-ray exposure these defects are initially ionized, and then they undergo a relaxation phase until reaching steady V_{OC} values. First, we underline that the difference in work function between the Ag and the AZO wide band gap semiconductor will likely generate a depletion layer at the Ag/AZO Schottky barrier.[86−88] This depletion zone will be sensitive to the level of defect localized in this junction. Furthermore, the V_{OC} drop followed by a slow relaxation of SP_1 in Figure 2b can be explained by a dynamic process of trap charging and discharging of optically active midgap states.[87,88] Indeed, due to contact between the Ag and AZO layer, ultrathin Ag−O−Zn chemical bonds can form upon the interaction between Ag and O. This interfacial bond will also lead to the generation of oxygen vacancies around the first few nanometers of AZO.[89] Oxygen vacancies near the Ag/ZnO interface were proposed to introduce interface defects below the conduction band minimum that act as traps. In fact, defect states above the Fermi level are available for accepting and trapping photoexcited electrons from the VBM of the AZO. Then, under beam exposure, a valence band-to-defect state optical transition will take place at the localized interface region. According to the fact that the actual V_{OC} is sensitive to imperfections from the interfaces and other stacked layers as well, the capture and release of a photogenerated electron will likely affect the V_{OC} response. We note that the fast drop and slow relaxation are related to the fast ionization of midgap defects under radiation and the slow discharge process of ionized traps, respectively. In addition, Rahamim et al.[90] have reported that the Ag−O−Zn interface states seem to present a long lifetime due to the long stabilization times of the photovoltage signal at the Ag/ZnO junction. Finally, we associate the low V_{OC} observed with the SP_2 sample to the presence of fewer interfacial defects at the Ag/ITO and/or ITO/AZO interfaces.

4. CONCLUSIONS

In this paper, we have shown how the iodide transport and ITO barrier layer affect the performance and stability of stacked Au/Ag/AZO/PCBM/HaP/NiO/ITO/glass solar cells. Our advanced operando HAXPES analyses have depicted that the release of iodide species from the HaP to the PCBM transport layer requires a certain threshold voltage (higher than the V_{OC}). The studies have also pointed out that the diffusion of iodide through the AZO/PCBM over time only happens following the gradient descent of iodide concentration. Furthermore, we have demonstrated that the migration of iodide from the HaP absorber toward the bimetal electrodes (Au/Ag) is unidirectional (irreversibility of the iodide ions migration). The results have suggested that the absorption of the iodide species by the Ag layer leads to the generation of AgI compound. By using the diffusion barrier layer between the Ag and AZO, we outstandingly validate that the ITO prevents the formation of AgI and leads to enhancement of the solar cell performances and stabilities. From all outcomes reported in this manuscript, we deeply believe this research will contribute to clarifying the deterioration mechanism that occurs in HaPSCs.

■ ASSOCIATED CONTENT

Supporting Information

The Supporting Information is available free of charge at https://pubs.acs.org/doi/10.1021/acs.chemmater.2c03162.

Current density−voltage ($J-V$) characteristic; operando HAXPES timeline illustration; HAXPES spectra of wide range survey scans; In $3d_{5/2}$, Sn $3d_{5/2}$, and O 1s core levels from the ITO barrier layer; Au 4f HAXPES core level spectra; X-ray and short time biasing effects on I 3d diffusion; time-dependent analysis of I 3d diffusion; Ag layer thickness impact on the I^- absorption of Ag; Zn 2p core level from AZO electron transport layer; band structure illustration before contact; experimental valence band spectra; and illustration of iodide diffusion just after interface contacts (PDF)

■ AUTHOR INFORMATION

Corresponding Authors

Ibrahima Gueye − *Synchrotron X-ray Group, Research Center for Advanced Measurement and Characterization, National Institute for Materials Science (NIMS), Sayo, Hyogo 679-5148, Japan; Synchrotron X-ray Station at SPring-8, Research Network and Facility Services Division (NIMS), Sayo, Hyogo 679-5148, Japan; Center for Synchrotron Radiation Research, Japan Synchrotron Radiation Research Institute (JASRI), Sayo, Hyogo 679-5198, Japan;* orcid.org/0000-0001-5296-3894; Email: ibrahima.gueye@spring8.or.jp

Yasuhiro Shirai − *Centre for Green Research on Energy and Environmental Materials, National Institute for Materials Science (NIMS), Tsukuba, Ibaraki 305-0044, Japan;* orcid.org/0000-0003-2164-5468; Email: SHIRAI.Yasuhiro@nims.go.jp

Osami Sakata − *Synchrotron X-ray Group, Research Center for Advanced Measurement and Characterization, National Institute for Materials Science (NIMS), Sayo, Hyogo 679-5148, Japan; Synchrotron X-ray Station at SPring-8, Research Network and Facility Services Division (NIMS), Sayo, Hyogo 679-5148, Japan; Center for Synchrotron Radiation Research, Japan Synchrotron Radiation Research Institute (JASRI), Sayo, Hyogo 679-5198, Japan;* orcid.org/0000-0003-2626-0161; Email: sakata.osami@spring8.or.jp

Authors

Takahiro Nagata − *Research Center for Functional Materials and International Center for Materials Nanoarchitectonics (WPI-MANA), National Institute for Materials Science (NIMS), Tsukuba, Ibaraki 305-0044, Japan; Graduate School of Science and Technology, Meiji University, Kawasaki, Kanagawa 214-8571, Japan;* orcid.org/0000-0002-8591-2943

Takashi Tsuchiya − *International Center for Materials Nanoarchitectonics (WPI-MANA), National Institute for Materials Science (NIMS), Tsukuba, Ibaraki 305-0044, Japan;* orcid.org/0000-0002-6950-6160

Dhruba B. Khadka − *Centre for Green Research on Energy and Environmental Materials, National Institute for Materials Science (NIMS), Tsukuba, Ibaraki 305-0044, Japan;* orcid.org/0000-0001-9134-3890

Masatoshi Yanagida − *Centre for Green Research on Energy and Environmental Materials, National Institute for Materials Science (NIMS), Tsukuba, Ibaraki 305-0044, Japan;* orcid.org/0000-0002-8065-7875

Downloaded from pubs.acs.org/cmatex/article-pdf/35/5/1948/2748132/cm2c03162.pdf by NATL INST FOR MATLS SCIENCE (NIMS) user on 10 November 2026

Okkyun Seo − *Synchrotron X-ray Group, Research Center for Advanced Measurement and Characterization, National Institute for Materials Science (NIMS), Sayo, Hyogo 679-5148, Japan; Synchrotron X-ray Station at SPring-8, Research Network and Facility Services Division (NIMS), Sayo, Hyogo 679-5148, Japan; Center for Synchrotron Radiation Research, Japan Synchrotron Radiation Research Institute (JASRI), Sayo, Hyogo 679-5198, Japan;* orcid.org/0000-0002-8732-0255

Kenjiro Miyano − *Centre for Green Research on Energy and Environmental Materials, National Institute for Materials Science (NIMS), Tsukuba, Ibaraki 305-0044, Japan;* orcid.org/0000-0002-5869-3087

Complete contact information is available at: https://pubs.acs.org/10.1021/acs.chemmater.2c03162

Notes

The authors declare no competing financial interest.

■ ACKNOWLEDGMENTS

Measurements were performed at SPring-8 with the approval of the NIMS Synchrotron X-ray Station at SPring-8 under proposal nos. 2020A4601, 2020A4652, and 2020A4653.

■ REFERENCES

(1) Li, D.; Zhang, D.; Lim, K.; Hu, Y.; Rong, Y.; Mei, A.; Park, N.; Han, H. A Review on Scaling Up Perovskite Solar Cells. *Adv. Funct. Mater.* **2021**, *31*, 2008621.

(2) Almora, O.; Baran, D.; Bazan, G. C.; Berger, C.; Cabrera, C. I.; Catchpole, K. R.; Erten-Ela, S.; Guo, F.; Hauch, J.; Ho-Baillie, A. W. Y.; Jacobsson, T. J.; Janssen, R. A. J.; Kirchartz, T.; Kopidakis, N.; Li, Y.; Loi, M. A.; Lunt, R. R.; Mathew, X.; McGehee, M. D.; Min, J.; Mitzi, D. B.; Nazeeruddin, M. K.; Nelson, J.; Nogueira, A. F.; Paetzold, U. W.; Park, N. G.; Rand, B. P.; Rau, U.; Snaith, H. J.; Unger, E.; Vaillant-Roca, L.; Yip, H. L.; Brabec, C. J. Device Performance of Emerging Photovoltaic Materials (Version 1). *Adv. Energy Mater.* **2021**, *11*, 2002774.

(3) Almora, O.; Baran, D.; Bazan, G. C.; Berger, C.; Cabrera, C. I.; Catchpole, K. R.; Erten-Ela, S.; Guo, F.; Hauch, J.; Ho-Baillie, A. W. Y.; Jacobsson, T. J.; Janssen, R. A. J.; Kirchartz, T.; Kopidakis, N.; Li, Y.; Loi, M. A.; Lunt, R. R.; Mathew, X.; McGehee, M. D.; Min, J.; Mitzi, D. B.; Nazeeruddin, M. K.; Nelson, J.; Nogueira, A. F.; Paetzold, U. W.; Park, N.-G.; Rand, B. P.; Rau, U.; Snaith, H. J.; Unger, E.; Vaillant-Roca, L.; Yip, H.-L.; Brabec, C. J. Device Performance of Emerging Photovoltaic Materials (Version 2). *Adv. Energy Mater.* **2021**, *11*, 2102526.

(4) Xiang, W.; Tress, W. Review on Recent Progress of All-Inorganic Metal Halide Perovskites and Solar Cells. *Adv. Mater.* **2019**, *31*, 1902851.

(5) Wu, T.; Qin, Z.; Wang, Y.; Wu, Y.; Chen, W.; Zhang, S.; Cai, M.; Dai, S.; Zhang, J.; Liu, J.; Zhou, Z.; Liu, X.; Segawa, H.; Tan, H.; Tang, Q.; Fang, J.; Li, Y.; Ding, L.; Ning, Z.; Qi, Y.; Zhang, Y.; Han, L. The Main Progress of Perovskite Solar Cells in 2020−2021. *Nano-Micro Lett.* **2021**, *13*, 152.

(6) De Wolf, S.; Holovsky, J.; Moon, S.-J.; Löper, P.; Niesen, B.; Ledinsky, M.; Haug, F.-J.; Yum, J.-H.; Ballif, C. J. Organometallic Halide Perovskites: Sharp Optical Absorption Edge and Its Relation to Photovoltaic Performance. *Phys. Chem. Lett.* **2014**, *5*, 1035−1039.

(7) Mosconi, E.; Amat, A.; Nazeeruddin, M. K.; Grätzel, M.; De Angelis, F. First-Principles Modeling of Mixed Halide Organometal Perovskites for Photovoltaic Applications. *J. Phys. Chem. C* **2013**, *117*, 13902.

(8) Kim, G.-W.; Petrozza, A. Defect Tolerance and Intolerance in Metal-Halide Perovskites. *Adv. Energy Mater.* **2020**, *10*, 2001959.

(9) Akkerman, Q. A.; Manna, L. What Defines a Halide Perovskite? *ACS Energy Lett.* **2020**, *5*, 604−610.

(10) Sajedi Alvar, M.; Blom, P. W.; Wetzelaer, G. J. A. Device Model for Methylammonium Lead Iodide Perovskite With Experimentally Validated Ion Dynamics. *Adv. Electron. Mater.* **2020**, *6*, 1900935.

(11) *Best solar cell efficiency chart*; https://www.nrel.gov/pv/cell-efficiency.html (Accessed June 30, 2022).

(12) Wu, M.; Haji Ladi, N.; Yi, Z.; Li, H.; Shen, Y.; Wang, M. Stability Issue of Perovskite Solar Cells under Real-World Operating Conditions. *Energy Technol.* **2020**, *8*, 1900744.

(13) Boyd, C. C.; Cheacharoen, R.; Leijtens, T.; McGehee, M. D. Understanding Degradation Mechanisms and Improving Stability of Perovskite Photovoltaics. *Chem. Rev.* **2019**, *119*, 3418−3451.

(14) Zhang, T.; Cheung, S. H.; Meng, X.; Zhu, L.; Bai, Y.; Ho, C. H. Y.; Xiao, S.; Xue, Q.; So, S. K.; Yang, S. Pinning Down the Anomalous Light Soaking Effect toward High-Performance and Fast-Response Perovskite Solar Cells: The Ion-Migration-Induced Charge Accumulation. *J. Phys. Chem. Lett.* **2017**, *8*, 5069−5076.

(15) Kang, D. H.; Park, N. G. On the Current-Voltage Hysteresis in Perovskite Solar Cells: Dependence on Perovskite Composition and Methods to Remove Hysteresis. *Adv. Mater.* **2019**, *31*, 1805214.

(16) Chen, C.; Song, Z.; Xiao, C.; Awni, R. A.; Yao, C.; Shrestha, N.; Li, C.; Bista, S. S.; Zhang, Y.; Chen, L.; Ellingson, R. J.; Jiang, C.-S.; Al-Jassim, M.; Fang, G.; Yan, Y. Arylammonium-Assisted Reduction of the Open-Circuit Voltage Deficit in Wide-Bandgap Perovskite Solar Cells: The Role of Suppressed Ion Migration. *ACS Energy Lett.* **2020**, *5*, 2560−2568.

(17) Liu, J.; Hu, M.; Dai, Z.; Que, W.; Padture, N. P.; Zhou, Y. Correlations between Electrochemical Ion Migration and Anomalous Device Behaviors in Perovskite Solar Cells. *ACS Energy Lett.* **2021**, *6*, 1003−1014.

(18) Moia, D.; Maier, J. Ion Transport, Defect Chemistry, and the Device Physics of Hybrid Perovskite Solar Cells. *ACS Energy Lett.* **2021**, *6* (4), 1566−1576.

(19) Eames, C.; Frost, J. M.; Barnes, P. R. F.; O'Regan, B. C.; Walsh, A.; Islam, M. S. Ionic transport in hybrid lead iodide perovskite solar cells. *Nat. Commun.* **2015**, *6*, 8.

(20) Yuan, Y.; Wang, Q.; Shao, Y.; Lu, H.; Li, T.; Gruverman, A.; Huang, J. Electric-Field-Driven Reversible Conversion Between Methylammonium Lead Triiodide Perovskites and Lead Iodide at Elevated Temperatures. *Adv. Energy Mater.* **2016**, *6*, 1501803.

(21) Weber, S. A. L.; Hermes, I. M.; Turren-Cruz, S.-H.; Gort, C.; Bergmann, V. W.; Gilson, L.; Hagfeldt, A.; Graetzel, M.; Tress, W.; Berger, R. How the Formation of Interfacial Charge Causes Hysteresis in Perovskite Solar Cells. *Energy Environ. Sci.* **2018**, *11* (9), 2404−2413.

(22) Wolff, C. M.; Caprioglio, P.; Stolterfoht, M.; Neher, D. Nonradiative Recombination in Perovskite Solar Cells: The Role of Interfaces. *Adv. Mater.* **2019**, *31*, 1902762.

(23) Wong, K. K.; Fakharuddin, A.; Ehrenreich, P.; Deckert, T.; Abdi-Jalebi, M.; Friend, R. H.; Schmidt-Mende, L. Interface-Dependent Radiative and Nonradiative Recombination in Perovskite Solar Cells. *J. Phys. Chem. C* **2018**, *122*, 10691−10698.

(24) Luo, D.; Su, R.; Zhang, W.; Gong, Q.; Zhu, R. Minimizing non-radiative recombination losses in perovskite solar cells. *Nat. Rev. Mater.* **2020**, *5*, 44−60.

(25) Yoo, J. J.; Seo, G.; Chua, M. R.; Park, T. G.; Lu, Y.; Rotermund, F.; Kim, Y. K.; Moon, C. S.; Jeon, N. J.; Correa-Baena, J. P.; Bulović, V.; Shin, S. S.; Bawendi, M. G.; Seo, J. Efficient perovskite solar cells via improved carrier management. *Nature* **2021**, *590*, 587−593.

(26) Daboczi, M.; Hamilton, I.; Xu, S.; Luke, J.; Limbu, S.; Lee, J.; McLachlan, M. A.; Lee, K.; Durrant, J. R.; Baikie, I.; Kim, J. S. Origin of Open-Circuit Voltage Losses in Perovskite Solar Cells Investigated by Surface Photovoltage Measurement. *ACS Appl. Mater. Interfaces* **2019**, *11* (50), 46808−46817.

(27) Krückemeier, L.; Rau, U.; Stolterfoht, M.; Kirchartz, T. How to Report Record Open-Circuit Voltages in Lead-Halide Perovskite Solar Cells. *Adv. Energy Mater.* **2020**, *10*, 1902573.

(28) Sood, M.; Urbaniak, A.; Kameni Boumenou, C.; Weiss, T. P.; Elanzeery, H.; Babbe, F.; Werner, F.; Melchiorre, M.; Siebentritt, S. Near surface defects: Cause of deficit between internal andexternal

Downloaded from pubs.acs.org/cmatex/article-pdf/35/5/1948/2748132/cm2c03162.pdf by NATL INST FOR MATLS SCIENCE (NIMS) user on 10 November 2026

open-circuit voltage in solar cells. *Prog. Photovolt., Res. Appl.* **2022**, *30*, 263−275.
(29) Stolterfoht, M.; Le Corre, V. M.; Feuerstein, M.; Caprioglio, P.; Koster, L. J. A.; Neher, D. Voltage-dependent photoluminescence and how it correlates with the fill factor and open-circuit voltage in perovskite solar cells. *ACS Energy Lett.* **2019**, *4*, 2887−2892.
(30) Choi, K.; Choi, H.; Min, J.; Kim, T.; Kim, D.; Son, S. Y.; Kim, G.-W.; Choi, J.; Park, T. A Short Review on Interface Engineering of Perovskite Solar Cells: A Self-Assembled Monolayer and Its Roles. *Sol. RRL* **2020**, *4*, 1900251.
(31) Rivkin, B.; Fassl, P.; Sun, Q.; Taylor, A.; Chen, Z.; Vaynzof, Y. Effect of Ion Migration-Induced Electrode Degradation on the Operational Stability of Perovskite Solar Cells. *ACS Omega* **2018**, *3*, 10042−10047.
(32) Gueye, I.; Shirai, Y.; Khadka, D. B.; Seo, O.; Hiroi, S.; Yanagida, M.; Miyano, K.; Sakata, O. Chemical and Electronic Investigation of Buried $NiO_{1-\delta}$, PCBM, PTAA/$MAPbI_{3-x}Cl_x$ Interfaces using Hard X-ray Photoelectron Spectroscopy and Transmission Electron Microscopy. *ACS Appl. Mater. Interfaces* **2021**, *13* (42), 50481−50490.
(33) Kato, Y.; Ono, L. K.; Lee, M. V.; Wang, S.; Raga, S. R.; Qi, Y. Silver Iodide Formation in Methyl Ammonium Lead Iodide Perovskite Solar Cells with Silver Top Electrodes. *Adv. Mater. Interfaces* **2015**, *2*, 1500195.
(34) Cheng, Y.; Liu, X.; Guan, Z.; Li, M.; Zeng, Z.; Li, H.-W.; Tsang, S.-W.; Aberle, A. G.; Lin, F. Revealing the degradation and self-healing mechanisms in perovskite solar cells by sub-bandgap external quantum efficiency spectroscopy. *Adv. Mater.* **2021**, *33*, 2006170.
(35) Boyd, C. C.; Cheacharoen, R.; Bush, K. A.; Prasanna, R.; Leijtens, T.; McGehee, M. D. Barrier Design to Prevent Metal-Induced Degradation and Improve Thermal Stability in Perovskite Solar Cells. *ACS Energy Lett.* **2018**, *3* (7), 1772−1778.
(36) Stolterfoht, M.; Caprioglio, P.; Wolff, C. M.; Márquez, J. A.; Nordmann, J.; Zhang, S.; Rothhardt, D.; Hörmann, U.; Amir, Y.; Redinger, A.; Kegelmann, L.; Zu, F.; Albrecht, S.; Koch, N.; Kirchartz, T.; Saliba, M.; Unold, T.; Neher, D. The impact of energy alignment and interfacial recombination on the internal and external open-circuit voltage of perovskite solar cells. *Energy Environ. Sci.* **2019**, *12* (9), 2778−2788.
(37) Schulz, P.; Cahen, D.; Kahn, A. Halide Perovskites: Is It All about the Interfaces? *Chem. Rev.* **2019**, *119*, 3349−3417.
(38) Hellmann, T.; Das, C.; Abzieher, T.; Schwenzer, J. A.; Wussler, M.; Dachauer, R.; Paetzold, U. W.; Jaegermann, W.; Mayer, T. The Electronic Structure of MAPI-Based Perovskite Solar Cells: Detailed Band Diagram Determination by Photoemission Spectroscopy Comparing Classical and Inverted Device Stacks. *Adv. Energy Mater.* **2020**, *10*, 2002129.
(39) Hüfner, S. *Photoelectron Spectroscopy, Principles and Applications*; Springer: Berlin/Heidelberg, 2003; DOI: 10.1007/978-3-662-09280-4.
(40) Suga, S.; Sekiyama, A. *Photoelectron Spectroscopy, Bulk and Surface Electronic Structures*; Springer-Verlag: Berlin/Heidelberg, 2014; DOI: 10.1007/978-3-642-37530-9.
(41) Gueye, I.; Le Rhun, G.; Renault, O.; Cooper, D.; Defay, E.; Barrett, N. Correlation of electrical characteristics with interface chemistry and structure in Pt/Ru/$PbZr_{0.52}Ti_{0.48}O_3$/Pt capacitors after post metallization annealing. *Appl. Phys. Lett.* **2018**, *113*, 132901.
(42) Gueye, I.; Le Rhun, G.; Renault, O.; Cooper, D.; Ceolin, D.; Rueff, J.-P.; Barrett, N. Operando hard X-ray photoelectron spectroscopy study of the Pt/Ru/ $PbZr_{0.52}Ti_{0.48}O_3$ interface. *Appl. Phys. Lett.* **2017**, *111*, 032906.
(43) Woicik, J. C. *Hard X-ray Photoelectron Spectroscopy (HAXPES)*; Springer Series in Surface Sciences; Springer: Berlin, 2016; DOI: 10.1007/978-3-319-24043-5.
(44) Tripathi, N.; Yanagida, M.; Shirai, Y.; Miyano, K. Improved performance of planar perovskite devices via inclusion of ammonium acid iodide (AAI) derivatives using a two step inter-diffusion process. *J. Mater. Chem. C* **2019**, *7*, 3447−3451.
(45) Khadka, D. B.; Shirai, Y.; Yanagida, M.; Masuda, T.; Miyano, K. Enhancement in efficiency and optoelectronic quality of perovskite thin films annealed in MACl vapor. *Sustainable Energy Fuels* **2017**, *1*, 755−766.
(46) Ueda, S.; Katsuya, Y.; Tanaka, M.; Yoshikawa, H.; Yamashita, Y.; Ishimaru, S.; Matsushita, Y.; Kobayashi, K. Present Status of the NIMS Contract Beamline BL15XU at SPring-8. *AIP Conf. Proc.* **2010**, *1234*, 403.
(47) Lin, F.; Liu, Y.; Yu, X.; Cheng, L.; Singer, A.; Shpyrko, O. G.; Xin, H. L.; Tamura, N.; Tian, C.; Weng, T.-C.; Yang, X.-Q.; Meng, Y. S.; Nordlund, D.; Yang, W.; Doeff, M. M. Synchrotron X-ray analytical techniques for studying materials electrochemistry in rechargeable batteries. *Chem. Rev.* **2017**, *117*, 13123−13186.
(48) Hirose, Y. *Materials Analysis Using Synchrotron Radiation, Research Report*; R&D Review of Toyota CRDL; Toyota: 2003.
(49) Terzano, R.; Denecke, M. A.; Falkenberg, G.; Miller, B.; Paterson, D.; Janssens, K. Recent advances in analysis of trace elements in environmental samples by X-ray based techniques (IUPAC Technical Report). *Pure Appl. Chem.* **2019**, *91*, 1029−1063.
(50) Tanuma, S.; Powell, C. J.; Penn, D. R. Calculations of electron inelastic mean free paths. V. Data for 14 organic compounds over the 50−2000 eV range. *Surf. Interface Anal.* **1994**, *21*, 165−176.
(51) Walton, J.; Wincott, P.; Fairley, N.; Carrick, A. *Peak Fitting with CasaXPS: A Casa Pocket Book*; Acolyte Science: Cheshire, 2010.
(52) Cao, J.; Zhao, Y. J.; Lin, H. L.; Xu, B. Y.; Chen, S. F. Facile synthesis of novel Ag/AgI/BiOI composites with highly enhanced visible light photocatalytic performances. *J. Solid State Chem.* **2013**, *206*, 38.
(53) Xue, W.; Peng, Z.; Huang, D.; Zeng, G.; Wen, X.; Deng, R.; Yang, Y.; Yan, X. In situ synthesis of visible-light-driven Z-scheme AgI/Bi_2WO_6 heterojunction photocatalysts with enhanced photocatalytic activity. *Ceram. Int.* **2019**, *45*, 6340−6349.
(54) Xue, M.; Liu, S.; Guo, J.; Guo, Q. Growth and electronic structure of Ag on polar MgO(111) films. *RSC Adv.* **2013**, *3*, 18916.
(55) Safo, I.; Werheid, M.; Dosche, C.; Oezaslan, M. The Role of Polyvinylpyrrolidone (PVP) as Capping and Structure-Directing Agent in the Formation of Pt Nanocubes. *Nanoscale Adv.* **2019**, *1*, 3095.
(56) Wu, S.; Chen, R.; Zhang, S.; Babu, B. H.; Yue, Y.; Zhu, H.; Yang, Z.; Chen, C.; Chen, W.; Huang, Y.; Fang, S.; Liu, T.; Han, L.; Chen, W. A chemically inert bismuth interlayer enhances long-term stability of inverted perovskite solar cells. *Nat. Commun.* **2019**, *10*, 1161.
(57) Gaarenstroom, S. W.; Winograd, N. Initial and final state effects in the ESCA spectra of cadmium and silver oxides. *J. Chem. Phys.* **1977**, *67*, 3500.
(58) Bagus, P. S.; Illas, F.; Pacchioni, G.; Parmigiani, F. Mechanisms responsible for chemical shifts of core-level binding energies and their relationship to chemical bonding. *J. Electron Spectrosc. Relat. Phenom.* **1999**, *100*, 215−236.
(59) Biesinger, M. C. Advanced analysis of copper X-ray photoelectron spectra. *Surf. Interface Anal.* **2017**, *49*, 1325−1334.
(60) Hendricks, C.; Mansour, A.; Fuentevilla, D.; Waller, G.; Ko, J.; Pecht, M. Copper dissolution in overdischarged lithium-ion cells: Xray photoelectron spectroscopy and x-ray absorption fine structure analysis. *J. Electrochem. Soc.* **2020**, *167*, 090501.
(61) Wong, A. S. W.; Krishnan, R. G.; Sarkar, G. X-ray photoelectron spectroscopy and Auger electron spectroscopy investigation on the oxidation resistance of plasma-treated copper leadframes. *J. Vac. Sci. Technol. A* **2000**, *18*, 1619.
(62) Li, J. W.; Dong, Q. S.; Li, N.; Wang, L. D. Direct Evidence of Ion Diffusion for the Silver-Electrode-Induced Thermal Degradation of Inverted Perovskite Solar Cells. *Adv. Energy Mater.* **2017**, *7*, 1602922.
(63) Xiang, D. L.; Liu, Z. R.; Wu, M. Q.; Liu, H. H.; Zhang, X. D.; Wang, Z.; Wang, Z. L.; Li, L. L. Enhanced Piezo-Photoelectric Catalysis with Oriented Carrier Migration in Asymmetric Au-ZnO Nanorod Array. *Small* **2020**, *16*, 1907603.
(64) Phung, N.; Al-Ashouri, A.; Meloni, S.; Mattoni, A.; Albrecht, S.; Unger, E. L.; Merdasa, A.; Abate, A. The Role of Grain Boundaries on Ionic Defect Migration in Metal Halide Perovskites. *Adv. Energy Mater.* **2020**, *10*, 1903735.
(65) McGovern, L.; Koschany, I.; Grimaldi, G.; Muscarella, L. A.; Ehrler, B. Grain Size Influences Activation Energy and Migration

Downloaded from pubs.acs.org/cmatex/article-pdf/35/5/1948/2748132/cm2c03162.pdf by NATL INST FOR MATLS SCIENCE (NIMS) user on 10 November 2026

Pathways in MAPbBr3 Perovskite Solar Cells. *J. Phys. Chem. Lett.* **2021**, *12*, 2423−2428.
(66) Buchholz, D. B.; Ma, Q.; Alducin, D.; Ponce, A.; Jose-Yacaman, M.; Khanal, R.; Medvedeva, J. E.; Chang, R. P. H. The Structure and Properties of Amorphous Indium Oxide. *Chem. Mater.* **2014**, *26*, 5401−5411.
(67) Bi, E.; Chen, H.; Xie, F.; Wu, Y.; Chen, W.; Su, Y.; Islam, A.; Grätzel, M.; Yang, X.; Han, L. Diffusion engineering of ions and charge carriers for stable efficient perovskite solar cells. *Nat. Commun.* **2017**, *8*, 15330.
(68) Yuan, Y.; Huang, J. Ion Migration in Organometal Trihalide Perovskite and Its Impact on Photovoltaic Efficiency and Stability. *Acc. Chem. Res.* **2016**, *49* (2), 286−293.
(69) Lin, D.; Xu, X.; Wang, J.; Zhang, T.; Xie, F.; Gong, L.; Chen, J.; Shi, T.; Shi, J.; Liu, P.; Xie, W. Construction of an Iodine Diffusion Barrier Using Network Structure Silicone Resin for Stable Perovskite Solar Cells. *ACS Appl. Mater. Interfaces* **2021**, *13*, 8138−8146.
(70) Wang, Q.; Shi, X.; Liu, E.; Xu, J.; Crittenden, J. C.; Zhang, Y.; Cong, Y. Preparation and Photoelectrochemical Performance of Visible-Light Active AgI/TiO_2 NTs Composite with Rich β-AgI. *Ind. Eng. Chem. Res.* **2016**, *55*, 4897−4904.
(71) Ding, C.; Fu, K.; Pan, Y.; Liu, J.; Deng, H.; Shi, J. Comparison of Ag and AgI-Modified ZnO as Heterogeneous Photocatalysts for Simulated Sunlight Driven Photodegradation of Metronidazole. *Catalysts* **2020**, *10*, 1097.
(72) Jiang, W.; An, C.; Liu, J.; Wang, S.; Zhao, L.; Guo, W.; Liu, J. Facile aqueous synthesis of β-AgI nanoplates as efficient visible-light-responsive photocatalyst. *Dalton Trans* **2014**, *43*, 300−305.
(73) Tang, Y.; Mak, C. H.; Liu, R.; Wang, Z.; Ji, L.; Song, H.; Tan, C.; Barrière, F.; Hsu, H. Y. In Situ Formation of Bismuth-Based Perovskite Heterostructures for High−Performance Cocatalyst−Free Photocatalytic Hydrogen Evolution. *Adv. Funct. Mater.* **2020**, *30*, 2006919.
(74) Xu, J. J.; Hu, Y. M.; Zeng, C.; Zhang, Y. H.; Huang, H. W. Polypyrrole decorated BiOI nanosheets: Efficient photocatalytic activity for treating diverse contaminants and the critical role of bifunctional polypyrrole. *J. Colloid Interface Sci.* **2017**, *505*, 719−727.
(75) Li, K.; Zhao, Y.; Zhang, P.; He, C.; Deng, J.; Ding, S.; Shi, W. Combined DFT and XPS investigation of iodine anions adsorption on the sulfur terminated (001) chalcopyrite surface. *Appl. Surf. Sci.* **2016**, *390*, 412−421.
(76) Dai, G. P.; Yu, J. G.; Liu, G. Synthesis and Enhanced Visible-Light Photoelectrocatalytic Activity of p-n Junction BiOI/TiO_2 Nanotube Arrays. *J. Phys. Chem. C* **2011**, *115*, 7339.
(77) Li, X.; Li, N.; Huang, Z.; Chen, Z.; Liang, G.; Yang, Q.; Li, M.; Zhao, Y.; Ma, L.; Dong, B.; Huang, Q.; Fan, J.; Zhi, C. Enhanced Redox Kinetics and Duration of Aqueous I_2/I^- Conversion Chemistry by MXene Confinement. *Adv. Mater.* **2021**, *33*, 2006897.
(78) Rocks, C.; Svrcek, V.; Maguire, P.; Mariotti, D. Understanding surface chemistry during $MAPbI_3$ spray deposition and its effect on photovoltaic performance. *J. Mater. Chem. C* **2017**, *5*, 902−916.
(79) Sztaberek, L.; Kang, J.; Chen, W.; Caruana, F. F.; Huz, K.; Robinson, J.; Amato, J.; Daniels, C. N.; McMahon, J. J. On the Role of the I_2/I^- Equilibrium in the Photocatalysis of Oxygen Reduction at Ag/AgI. *ACS Energy Lett.* **2016**, *1* (2), 409−413.
(80) Dong, Q.; Ho, C. H. Y.; Yu, H.; Salehi, A.; So, F. Defect passivation by fullerene derivative in perovskite solar cells with aluminum-doped zinc oxide as electron transporting layer. *Chem. Mater.* **2019**, *31*, 6833−6840.
(81) Philippe, B.; Jacobsson, T. J.; Correa-Baena, J.-P.; Jena, N. K.; Banerjee, A.; Chakraborty, S.; Cappel, U. B.; Ahuja, R.; Hagfeldt, A.; Odelius, M.; Rensmo, H. Valence Level Character in a Mixed Perovskite Material and Determination of the Valence Band Maximum from Photoelectron Spectroscopy: Variation with Photon Energy. *J. Phys. Chem. C* **2017**, *121*, 26655−26666.
(82) Khadka, D. B.; Shirai, Y.; Yanagida, M.; Miyano, K. Insights into Accelerated Degradation of Perovskite Solar Cells under Continuous Illumination Driven by Thermal Stress and Interfacial Junction. *ACS Appl. Energy Mater.* **2021**, *4* (10), 11121−11132.
(83) Thampy, S.; Zhang, B.; Hong, K.-H.; Cho, K.; Hsu, J. W. P. Altered Stability and Degradation Pathway of $CH_3NH_3PbI_3$ in Contact with Metal Oxide. *ACS Energy Lett.* **2020**, *5* (4), 1147−1152.
(84) Chen, B.; Yang, M.; Priya, S.; Zhu, K. Origin of J-V Hysteresis in Perovskite Solar Cells. *J. Phys. Chem. Lett.* **2016**, *7* (5), 905−917.
(85) Li, C.; Tscheuschner, S.; Paulus, F.; Hopkinson, P. E.; Kießling, J.; Köhler, A.; Vaynzof, Y.; Huettner, S. Iodine Migration and its Effect on Hysteresis in Perovskite Solar Cells. *Adv. Mater.* **2016**, *28*, 2446−2454.
(86) Ishii, M.; Yoshino, Y.; Takarabe, K.-i.; Shimomura, O. Direct observation of local structure of DX center by capacitance X-ray absorption fine structure. *Phys. B Condens. Matter* **1999**, *273*−*274*, 774−777.
(87) Ishii, M.; Yoshino, Y.; Takarabe, K.-i.; Shimomura, O. X-ray induced photoemission of a localized electron and its application to site-selective x-ray absorption fine structure measurement. *J. Appl. Phys.* **2000**, *88*, 3962.
(88) Ishii, M. Site-specific x-ray absorption spectroscopy of electron traps by x-ray-induced displacement current measurement. *Phys. Rev. B* **2002**, *65* (8), 085310.
(89) Jain, M.; Manju; Kumar, R.; Won, S. O.; Chae, K. H.; Vij, A.; Thakur, A. Defect states and kinetic parameter analysis of ZnAl2O4 nanocrystals by X-ray photoelectron spectroscopy and thermoluminescence. *Sci. Rep* **2020**, *10*, 385.
(90) Rahamim, M.; Cohen, H.; Edri, E. Chemistry and Charge Trapping at the Interface of Silver and Ultrathin Layers of Zinc Oxide. *ACS Appl. Mater. Interfaces* **2021**, *13* (41), 49423−49432.

Downloaded from pubs.acs.org/cmatex/article-pdf/35/5/1948/2748132/cm2c03162.pdf by NATL INST FOR MATLS SCIENCE (NIMS) user on 10 November 2026

https://doi.org/10.1021/acs.chemmater.2c03162
Chem. Mater. 2023, 35, 1948−1960